The Effect of Solidification Rate on the Growth of Small Fatigue Cracks in a Cast 319-Type Aluminum Alloy

M.J. CATON, J.W. JONES, J.M. BOILEAU, and J.E. ALLISON

A study was conducted to investigate the effect of solidification rate on the growth behavior of small fatigue cracks in a 319-type aluminum alloy, a common Al-Si-Cu alloy used in automotive castings. Fatigue specimens were taken from cast material that underwent a hot isostatic pressing (HIP) process in order to eliminate shrinkage pores and to facilitate the observation of surface-initiated cracks by replication. Naturally initiated surface cracks ranging in length from 17 μm to 2 mm were measured using a replication technique. Growth rates of the small cracks were calculated as a function of the elastic stress-intensity-factor range (ΔK). Long-crack growth-rate data (10 mm $\leq$ length $\leq$ 25 mm) were obtained from compact-tension (CT) specimens, and comparison to the small-crack data indicates the existence of a significant small-crack effect in this alloy. The solidification rate is shown to have a significant influence on small-crack growth behavior, with faster solidification rates resulting in slower growth rates at equivalent ΔK levels. A stress-level effect is also observed for both solidification rates, with faster growth rates occurring at higher applied-stress amplitudes at a given ΔK. A crack-growth relation proposed by Nisitani and others is modified to give reasonable correlation of small-crack growth data to different solidification rates and stress levels.

I. INTRODUCTION

OVER the past decade, the automotive industry has increasingly employed cast aluminum alloys as a replacement for cast iron in the production of engine components. This material substitution results in a substantial weight reduction and, consequently, enhanced fuel efficiency. The 319 aluminum family is commonly used in casting engine blocks and cylinder heads. The increased use of these Al-Si-Cu alloys in demanding structural applications requires a better understanding of their response to fatigue loading. The influence of processing parameters on fatigue properties is of particular interest.

The microstructural feature which plays perhaps the most dominant role in determining the fatigue properties of a cast material is porosity. Aluminum castings contain shrinkage pores which vary in size and distribution depending upon the rate at which the metal is solidified, with faster solidification generally resulting in a lower fraction of smaller pores than with slower solidification rates. Under fatigue loading, a shrinkage pore acts as a stress raiser and serves as a prime site for crack nucleation. Several investigations of the fatigue behavior of cast aluminum alloys have shown that fatigue cracks initiate predominantly from pores.[1–4] It is further concluded in these studies that, at a given stress, the number of cycles required to initiate a crack is small relative to the total fatigue life. That is, the fatigue life is dominated by the propagation of a crack that initiates from a pore, or a cluster of closely spaced pores, after a relatively small number of cycles.

If the initiation life (N_i) of a cast aluminum specimen is assumed to be a negligible fraction of the total fatigue life (N_f), then a quantitative prediction of the fatigue life can be made by calculating the propagation life (N_p) using a fracture-mechanics analysis. Couper *et al.*[1] used a linear elastic fracture-mechanics (LEFM) analysis to predict the fatigue life in an Al-7Si-0.4Mg casting alloy. Here, the Paris equation, $da/dN = C(\Delta K_{\text{eff}})^m$, was expanded and integrated from an initial crack size (a_i) to the critical crack size for failure (a_f) to calculate the propagation life. This calculated propagation life was then compared to the actual fatigue life. In this analysis, ΔK_{eff} is the effective stress-intensity-factor range which accounts for crack closure, and C and m are material constants determined empirically. The pore from which the fatal crack initiated was measured from the fracture surface, and an equivalent initial crack size was determined. The life predictions from this study were in reasonable agreement with the actual lifetimes but tended to be nonconservative estimates, especially at higher stresses.

Skallerud *et al.*[2] conducted a similar life-prediction study on a cast Al-7Si-0.4Mg alloy using a LEFM analysis and considering single and multiple pore configurations leading to crack initiation. This model considers the initiation life to be negligible and calculates the propagation life from the crack-growth relationship

$$\frac{da}{dN} = C(\Delta K_{\text{eff}}^m - K_{th,\text{eff}}^m) \qquad [1]$$

where $\Delta K_{th,\text{eff}}$ represents the effective stress-intensity-factor range threshold. The values of ΔK_{eff}, $\Delta K_{th,\text{eff}}$, C, and m were determined from closure-corrected long-crack growth data. Similar to the trend seen by Couper *et al.*, the life predictions of this model were in reasonable agreement with the experimental lifetimes but were somewhat nonconservative, especially at higher stresses.

A reason for the overestimates of fatigue life from these

M.J. CATON, Graduate Student/Research Assistant, Department of Materials Science and Engineering, and J. WAYNE JONES, Professor of Materials Science and Engineering, and Associate Dean for Undergraduate Education, College of Engineering, are with the University of Michigan, Ann Arbor, MI 48109. J.M. BOILEAU, Research Engineer, and J.E. ALLISON, Senior Staff Technical Specialist, are with the Materials Science Department, Ford Research Laboratories, Ford Motor Company, Dearborn, MI 48124-2053.

Manuscript submitted July 7, 1998.

two analyses could be the existence of a small-crack effect. The small-crack effect refers to the general observation that, under cyclic loading, small cracks grow at significantly faster rates than long cracks (at ≥2 mm) and at stress intensities less than the long-crack threshold stress-intensity factor, determined using a LEFM approach.[5,6] A crack can be categorized as "small" based upon several different definitions, but, in general, a crack less than ~1 to 2 mm in dimension can be considered a small crack. Much has been written about the physical basis for the differences in growth rates for large and small cracks, and three reasons are commonly proposed: (1) crack closure, (2) breakdown in metallurgical similitude, and (3) plasticity effects. The reader is referred to Newman *et al.*[7] and Tanaka and Akiniwa[8] for concise summaries of these concepts as they relate to the small-crack phenomenon. A small-crack effect has been observed and well documented in several wrought aluminum alloys,[9,10,11] but comparatively little has been written about experimental observation of this phenomenon in cast aluminum alloys. Shiozawa *et al.*,[12] O'Connor and Plumtree,[13] and Gungor and Edwards[14] have studied the initiation and growth of small cracks in squeeze-cast aluminum alloys. In the squeeze casting process, a pressure (~50 to 140 MPa) is applied to the molten metal throughout the entire duration of solidification. This yields essentially pore-free castings with very fine grains (as small as 100 to 200 μm) and superior mechanical properties when compared to castings from conventional gravity and counter-gravity processes. However, microstructures similar to those seen in gravity castings are achieved, and the behavior of fatigue crack growth in these alloys offers valuable insights for comparative purposes. Some studies of small fatigue cracks in aluminum alloys produced by die casting or permanent mold casting have also been reported. Ting reported accelerated growth of short cracks in a cast 319 aluminum alloy where the cracks grew from sharp notches ($K_t = 4.85$ and 11) and had a through-thickness length of 5 mm and crack depths ≥0.2 mm.[4] Seniw *et al.* have recently reported a small-crack effect in a die-cast A356 aluminum alloy.[15]

The existence of a small-crack effect in cast aluminum alloys could explain the overestimates of fatigue properties in the models proposed by Couper *et al.* and Skallerud *et al.* Both models rely upon growth data from long cracks to estimate the propagation behavior of a fatal crack growing from the dimensions of an initiating pore (~10 to 200 μm) to the final critical size adequate to cause failure. This would certainly include a period during which the crack could behave as a "small" crack. Reduced levels of crack closure have long been considered as a possible cause for the accelerated growth of small cracks.[16] However, both models considered crack closure in their analyses and still yielded overestimates of life. Skallerud *et al.* further modified their model by introducing an effective crack length (a_0) into the stress-intensity solution,

$$\Delta K_{\text{eff}} = \Delta\sigma_{\text{eff}}\sqrt{\pi(a + a_0)} \cdot F \qquad [2]$$

where F is a geometric correction factor. This is an approach proposed by El Haddad *et al.*[17] to predict the behavior of small cracks, where a_0 is a constant derived from ΔK_{th} and the fatigue limit. The life predictions resulting from this modified model were conservative.

Since crack propagation is theorized to account for a significant portion of the fatigue life in cast aluminum, accurate material models require consideration of small-crack growth behavior. Using long-crack growth-rate measurements as a basis for estimating the behavior of small cracks can yield inaccurate life predictions. Further, small cracks may be influenced by certain microstructural or loading parameters which exhibit no apparent effect on long cracks. It is the objective of this article to establish small-crack growth-rate relations using a LEFM approach and to determine if a small-crack effect is evident in this cast 319 aluminum alloy. Since castings of complex shape, such as automotive engine components, experience a wide range of solidification rates throughout their cross section, it is a further objective of this article to determine the extent to which the solidification rate affects the growth behavior of small fatigue cracks.

II. EXPERIMENTAL

A. *Material*

The alloy used in this study is from the 319 Al family and will be termed W319 within this article. The average composition of the W319 alloy is given in Table I. For comparison, the compositional ranges for the standard Aluminum Association 319 alloy (AA319) are included. Notably, the W319 alloy possesses increased Si, lower Fe, and an addition of Sr when compared to AA319.

The wedge-shaped casting shown schematically in Figure 1 was designed to simulate the broad range of solidification rates experienced in a cast engine component. The wedge has a tapered geometry, with the thickness dimension increasing from 1.3 to 7.6 cm. A copper chill block is located at the nose of the wedge, as indicated in Figure 1, and the time for the cast metal to fully solidify increases uniformly with distance from the copper chill. In general, the microstructure of the solidified casting becomes progressively coarser with increased distance from the copper chill.

In order to examine the effect of solidification rate on the propagation of small fatigue cracks, specimens were sampled from two regions within the wedge casting. Rectangular bars were cut from a region 3.2 to 5.1 cm from the chill, where the average time for complete solidification is ~44 seconds and the average secondary dendrite arm spacing (SDAS) is ~23 μm. Throughout this article, specimens from this region are referred to as the "fine" condition. Rectangular bars were also cut from a region 21.6 to 24.1 cm from the chill, where

Table I. Compositions of W319 and AA319

Element	W319 (Wt Pct)	AA319.0 (Wt Pct)
Si	7.43	5.5 to 6.5
Cu	3.33	3.0 to 4.0
Mg	0.22	0.10
Mn	0.24	0.50
Fe	0.38	1.0
Ni	0.01	0.35
Ti	0.12	0.25
Zn	0.13	1.0
Sr	0.03	—
Cr	0.03	—
Al	balance	balance

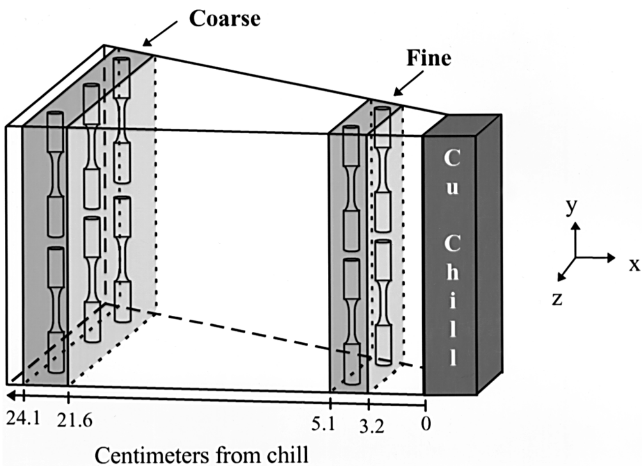

Fig. 1—A schematic representation of the wedge casting from which the fatigue and tensile specimens were sampled. The average time for complete solidification is ~44 s in the region indicated as fine and ~2600 s in the region indicated as coarse.

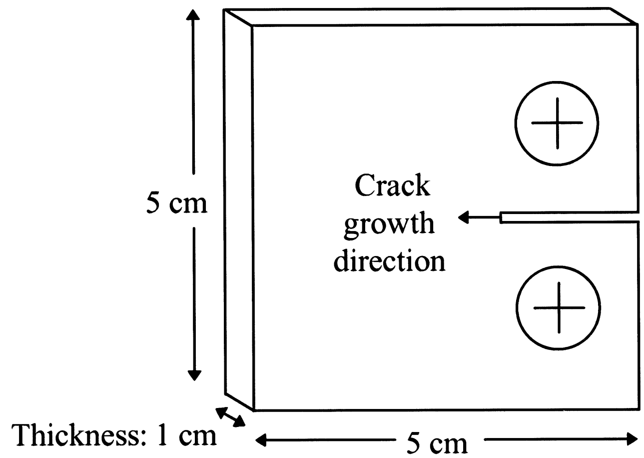

Fig. 2—A schematic of the CT specimen used to measure long fatigue crack growth. The specimens were sampled from the wedge casting of Fig. 1 such that the crack growth direction is away from the Cu chill in the *x*-*z* plane and the load axis is parallel to the vertical direction (*y* direction).

the average solidification time is ~2600 seconds (43 minutes) and the average SDAS is ~100 μm. Specimens from this region are, henceforth, referred to as the "coarse" condition.

All of the specimens examined in this study were sampled from wedge castings that underwent a hot isostatic pressing (HIP) procedure at 480 °C and 105 MPa for 3 hours. This procedure reduces the shrinkage porosity to a negligible level as measured using metallographic techniques. A T7 heat treatment, consisting of an 8-hour solution treatment at 495 °C followed by a boiling water quench (~90 °C) and 4 hours of aging at 260 °C, was given to the rectangular samples prior to machining to the final dimensions specified subsequently. The longitudinal axes of the specimens coincide with the vertical dimension of the wedge casting, as illustrated in Figure 1. Since the solidification rate is essentially uniform in the vertical dimension of the wedge, a given fatigue specimen possesses a uniform microstructure throughout its entire length.

B. *Testing Procedures*

Tensile tests were conducted for the fine and coarse microstructures using a servohydraulic test frame in stroke control and using an initial strain rate of 1.3 mm/min. The stress *vs* strain data were digitally acquired, and the 0.2 pct offset yield strength (σ_{yield}) and ultimate tensile strength (σ_t) were calculated in accordance with ASTM E8.

Compact-tension (CT) specimens, like that illustrated in Figure 2, were machined from the fine and coarse regions of the wedge casting, and fatigue crack growth rates were measured for through-thickness long cracks ranging in length from ~10 to 25 mm. The specimens were taken from the wedge casting shown in Figure 1, such that the cracks grew in the x-z plane and in the direction away from the Cu chill. A commercial testing laboratory was used for these studies. Crack growth rates were recorded as a function of the elastic stress-intensity-factor range (ΔK) as well as the effective stress-intensity-factor range (ΔK_{eff}), which was determined by the ASTM technique described in Reference 18. Tests were conducted in a laboratory environment at room temperature and at a stress ratio (R) of 0.1 and a frequency of 20 Hz, in accordance with the requirements of ASTM E 647-95.

All fatigue tests for which small-crack growth-rate measurements were performed were conducted in a laboratory environment at room temperature (23 °C) under load-controlled, uniaxial tension using a servohydraulic test frame. Constant-amplitude, fully reversed loading was applied ($R = -1$) at a frequency of 30 Hz to all specimens. Tests were conducted at two stress amplitudes, with maximum nominal stresses of 100 and 140 MPa. Fully-reversed loading was used because naturally initiated surface cracks initiate in fewer cycles under this condition than at positive stress ratios. This makes it much easier to monitor cracks using replication. Monitoring naturally initiated small-crack growth at positive R ratios is an exceedingly more difficult experimental task and is left to be addressed in future studies.

A schematic drawing of the fatigue specimen from which small cracks were examined is shown in Figure 3. The specimen is cylindrical, with two 28-mm-radius notches ground into opposite sides of the gage section. The elastic stress concentration factor due to the notches is approximated from Peterson's handbook[19] to be $K_t \cong 1.04$. This geometry was chosen because it provides a discrete plane of minimum cross-sectional area. Consequently, fatigue cracks are most likely to nucleate on or very near this plane of maximum stress, which facilitates locating and monitoring the growth of small cracks. The notched surfaces were hand polished to a 1 μm finish using a diamond paste. Initiation and growth of small cracks were monitored by employing standard replication techniques, [20] whereby cellulose acetate replicas were periodically taken from the two notched surfaces during fatigue testing by interrupting the tests and applying static holds of 70 pct $\sigma_{\max}$. Replicas were examined optically to determine crack lengths as a function of cycles. Cracks with surface lengths from 17 μm to 2 mm were detected. For the purpose of analysis, the projection of crack length in the direction normal to the stress axis was used, as illustrated in Figure 4(a). Figure 4(b) illustrates the typical

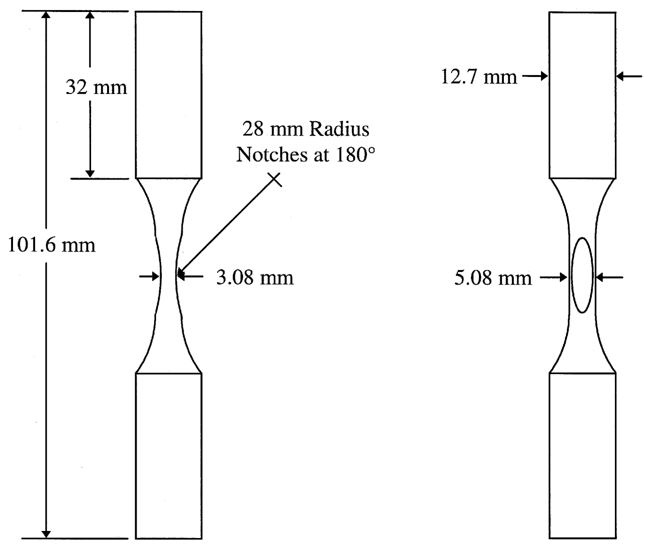

Fig. 3—A schematic drawing of the fatigue specimen used to examine small-crack growth. Plastic replicas were taken from the two notched surfaces within the gage section.

progression of crack growth with increased cycles, as detected by the replication technique.

C. *Data Analysis*

Using the crack length *vs* cycles data measured from the replicas, crack growth rates (da/dN) were determined by a standard seven-point, sliding polynomial method. The stress-intensity-factor range corresponding to a given crack length was calculated using a solution presented by Newman and Raju for a surface crack growing in a finite plate.[21] The equation for ΔK under uniaxial loading takes the form of

$$\Delta K = \Delta\sigma \cdot F \cdot \sqrt{\pi \frac{a}{Q}} \qquad [3]$$

where Q is a shape factor, F is a boundary correction factor, and a denotes the crack depth. A schematic illustration of a surface crack present in a fatigue specimen is given in Figure 5. In determining ΔK, the crack shape was assumed to be semicircular where the crack depth was estimated to be equal to half of the crack length, and the stress intensity was determined at the interior front of the small crack where the parametric angle (ϕ) was assigned the value of 90 deg. Only the tensile portion of the applied stress range ($\Delta\sigma$) was used in Eq. [3], since it is thought that only this portion of the loading cycle contributes to crack growth. Since ΔK is calculated at the interior front of the crack, the crack growth rates in this article are reported as da/dN. Since a is assumed to be equal to the measured value of c, the growth rates could equivalently be reported as dc/dN.

III. RESULTS

A. *Microstructure*

A schematic drawing of a planar cut of the wedge casting is given in Figure 6(a), showing the grain morphology that results from the directional solidification. The material very

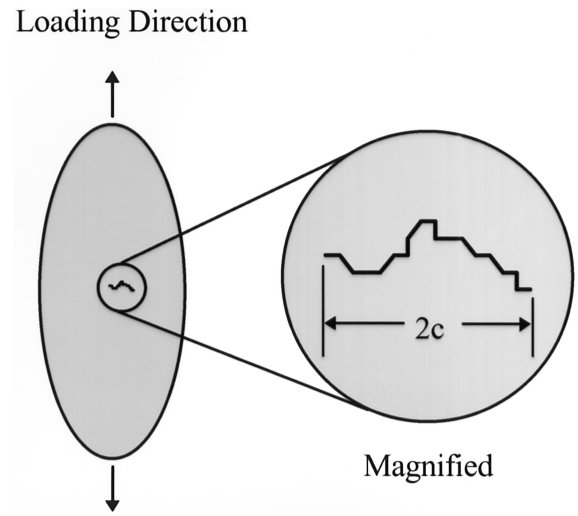

(*a*)

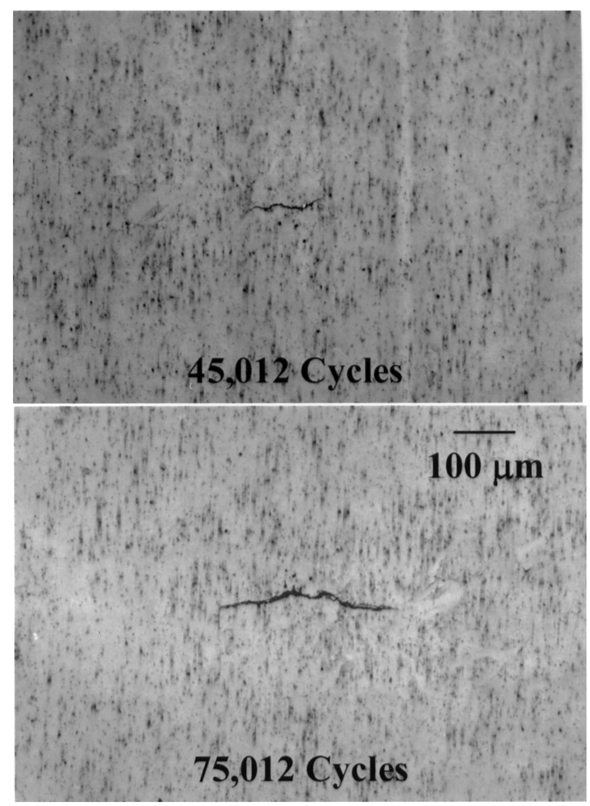

(*b*)

Fig. 4—(*a*) Schematic illustration of a typical small crack as it appears on the replication tape. Crack length, $2c$, is measured as the crack's projection normal to the loading direction. (*b*) Two replicas of the same small crack illustrating the growth experienced from 45,012 to 75,012 cycles. This crack propagated in the coarse microstructure at 100 MPa.

near the copper chill solidifies quickly and primarily exhibits a columnar morphology with an orientation consistent with the direction of heat removal, as indicated by the arrows in the figure. At distances greater than ~9 cm from the copper chill (measured as x in the figure), the grains are relatively equiaxed in morphology. Therefore, the fatigue specimens from the fine region of the wedge casting (3.2 cm $< x <$ 5.1 cm) possessed some degree of columnar grains and long

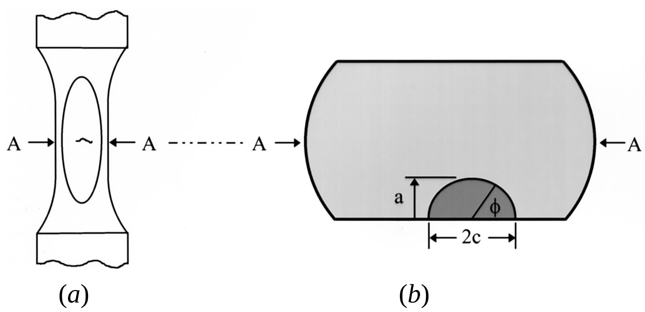

Fig. 5—Schematic illustration of a small surface crack as viewed (*a*) from the side of the fatigue specimen and (*b*) from the interior cross-sectional plane of the specimen. A semicircular crack shape is assumed where $a = c$.

needle-like dendrites, whose orientation was random with respect to where the two notches were placed. The average dimensions of the grains in the fine region of the wedge are approximately 0.47 mm by 1.3 mm, and a photomicrograph of the grains in this region is shown in Figure 6(c). The fatigue specimens from the coarse region of the casting (21.6 cm $< x <$ 24.1 cm) possessed equiaxed grains with an average diameter of approximately 1.6 mm. A photomicrograph of the grains in the coarse region is given in Figure 6(b).

Figure 7 shows micrographs of the coarse and fine microstructures taken using a scanning electron microscope (SEM). In Figure 7(a), the light-gray regions are the dendrite arms of the primary α phase. The interdendritic regions consist of Al-Si eutectic with the Si particles (black) contained in an α matrix. The SDAS of samples removed from the thick region of the casting (coarse) is 100 ± 25 μm. Also visible in the coarse microstructure are intermetallic phases, which appear white in the micrograph. The two irregular-shaped intermetallics on the right side of Figure 7(a) are termed the "Chinese-script" phase and have the composition $Al_{15}(Mn,Fe)_3Si_2$. In the coarse microstructure, these script-phase particles can have dimensions on the order of several hundred microns. The white intermetallic particles on the left side of Figure 7(a) are Al_2Cu precipitates, which can be on the order of 50 to 200 μm in dimension in the coarse microstructure. Figure 7(b) shows the much smaller and less-distinct dendrite arms in the fine microstructure. The

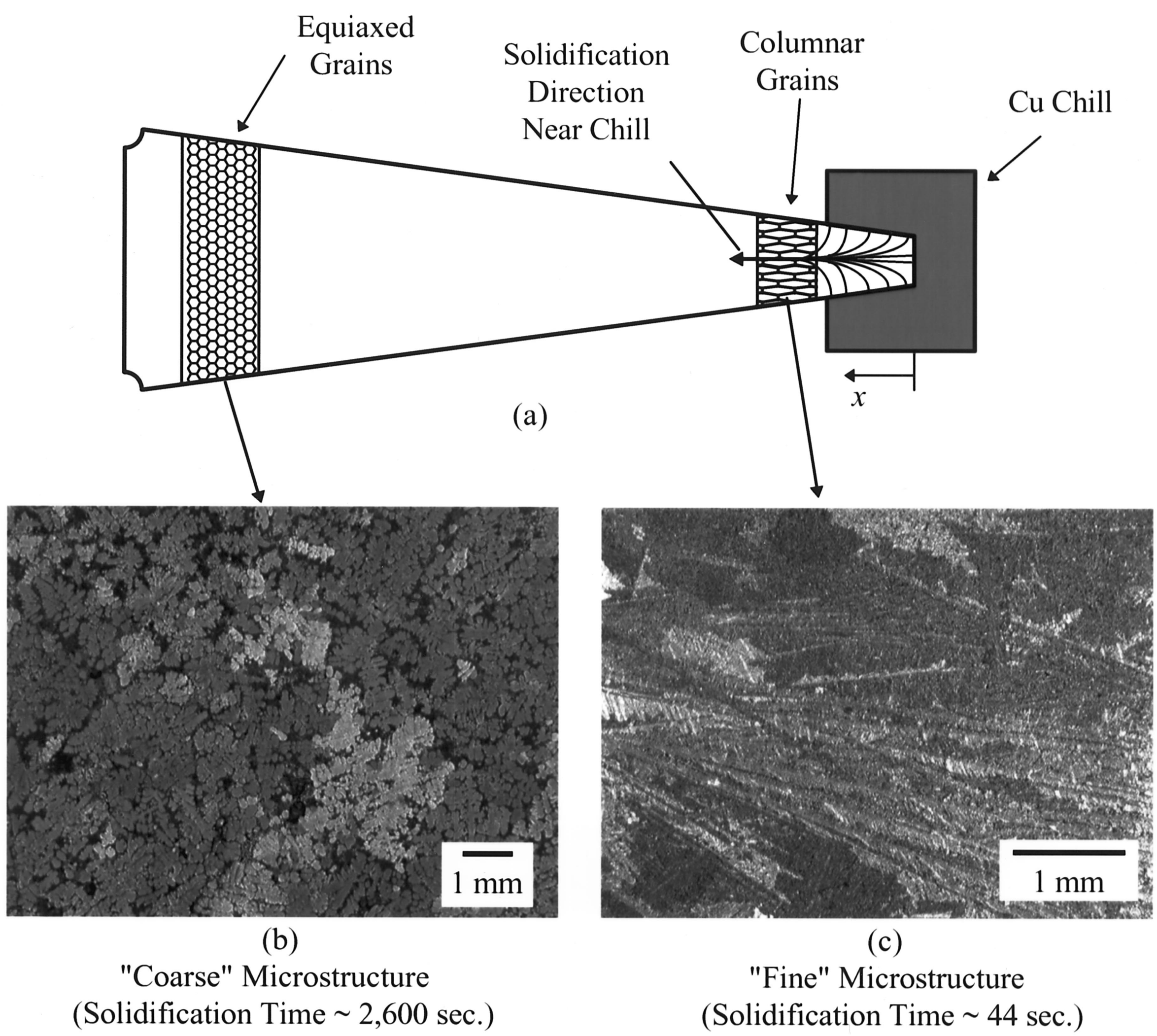

Fig. 6—(*a*) Schematic illustration of the grain morphology throughout a planar cross section of the wedge casting. Photos of the grain morphology within the (*b*) thick or coarse and (*c*) thin or fine regions of the wedge casting from which fatigue specimens were sampled.

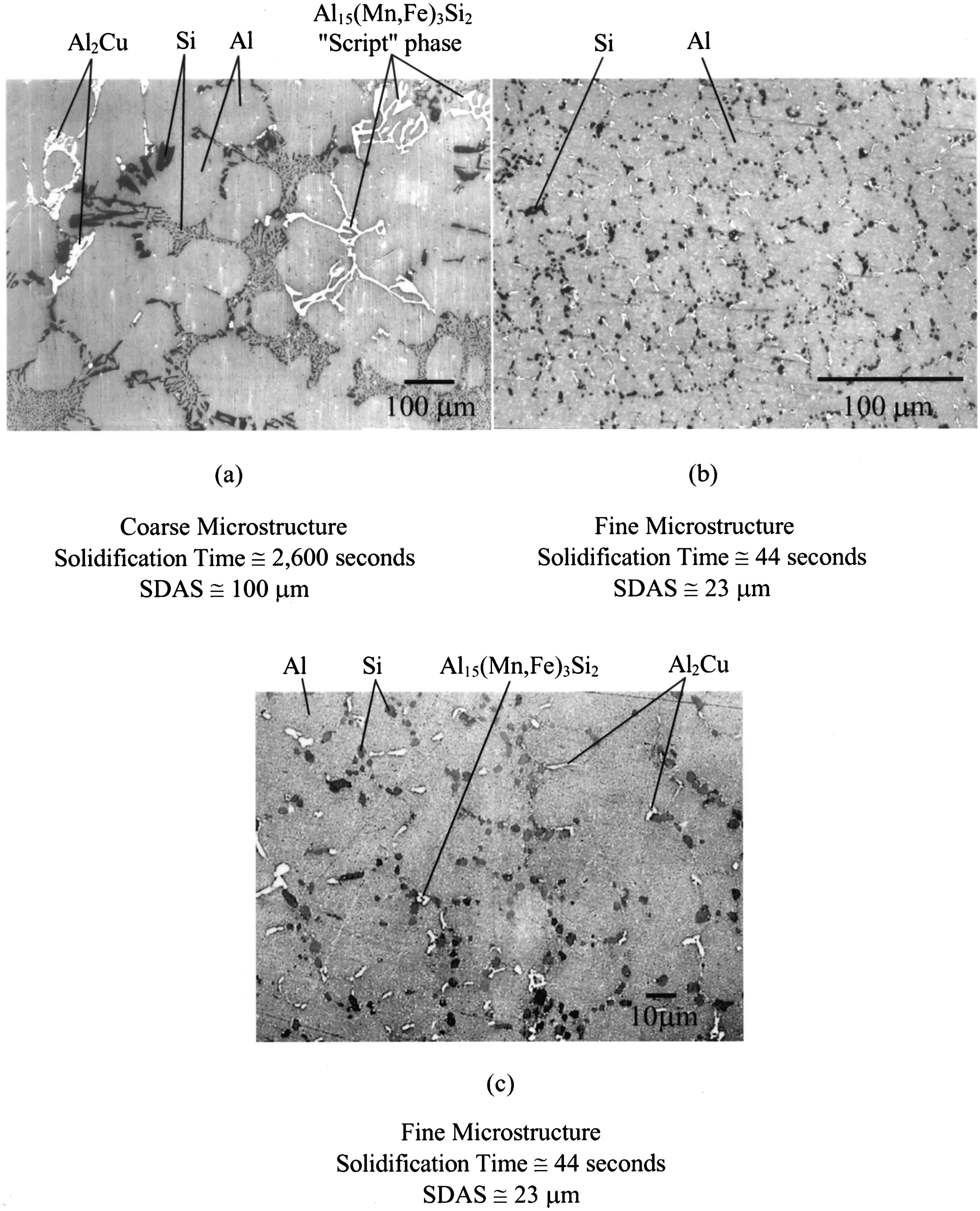

Fig. 7—SEM micrographs showing the dendritic microstructures of the (*a*) coarse and (*b*) and (*c*) fine regions of the wedge casting from which the fatigue specimens were sampled.

SDAS of samples removed from the thin region of the casting (fine) is 23 ± 7 μm. The Al_{15} (Mn, Fe)$_3$Si$_2$ and Al_2Cu intermetallics seen in the coarse microstructure are also present in the fine microstructure, but have dimensions on the order of 10 μm. These intermetallics, as well as the morphology of the Si, can be seen at higher magnification in Figure 7(c).

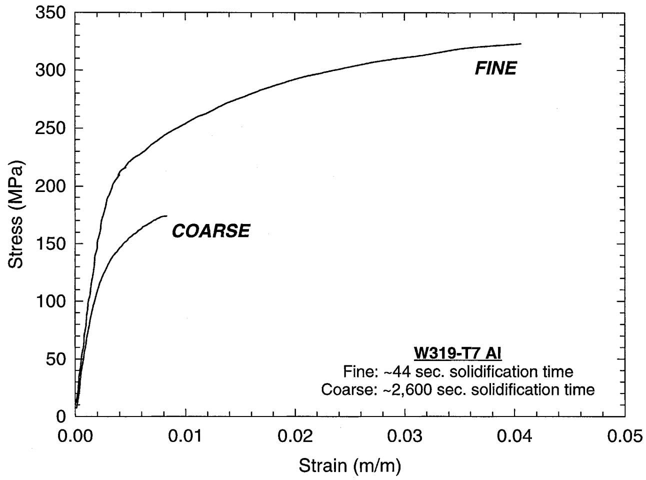

Fig. 8—Typical monotonic engineering stress-strain curves for the coarse and fine microstructures.

B. *Monotonic Tensile Behavior*

Figure 8 shows typical engineering stress *vs* strain curves for the coarse and the fine microstructures. The solidification rate has a significant effect on the monotonic tensile behavior of the cast alloy, with faster solidification resulting in greater strength and ductility. The calculated values of yield strength, ultimate tensile strength, and plastic strain to failure for the two microstructures are given in Table II. The average yield strength of the fine microstructure (202 MPa) is ~31 pct greater than that of the coarse microstructure (154 MPa), while the average ultimate tensile strength of the fine microstructure (312 MPa) is ~69 pct greater than that of the coarse microstructure (185 MPa). The plastic strain to failure in the fine microstructure (5.9 pct) is ~9.8 times greater than that of the coarse microstructure (0.6 pct). These values were measured for specimens which underwent HIP. The tensile behavior of this alloy is slightly different for the condition where HIP is not performed.

Table II. Summary of the Properties and Characteristics of the Two Microstructural Conditions Tested in This Study; Properties Measured for Specimens That Underwent HIP

Microstructural Condition →	Fine	Coarse
Distance from copper chill	3.2 to 5.1 cm	21.6 to 24.1 cm
Average solidification time	44 s	2600 s
Grain morphology	columnar	equiaxed
Approximate grain dimensions	0.5 × 1.3 mm	1.6 mm
SDAS	23 μm	100 μm
Average tensile yield strength	202 MPa	154 MPa
Average ultimate tensile strength	312 MPa	185 MPa
Average plastic strain to failure, ε_p (pct)	5.9	0.6

C. *Crack Initiation*

In the coarse microstructure, the small fatigue cracks nucleated predominantly from large script–phase intermetallic particles ($Al_{15}(Mn, Fe)_3Si_2$). The SEM micrographs in Figure 9 illustrate two examples of such a nucleation site. As seen in Figure 9(a), some of these cracks initially grew in directions conforming to the shape of the intermetallic particle and, once beyond the particle, grew essentially perpendicular to the loading direction. Cracks were observed to grow both within intermetallic particles as well as along particle/matrix interfaces. In the fine microstructure, the formation of slip bands was observed on the specimen surfaces and the fatigue cracks initiated predominantly from these slip bands. An example of such a crack is shown in Figure 10. At the stress amplitude of 140 MPa, multiple slip bands were observed on the specimen surfaces at various orientations relative to the loading direction. Figure 11 illustrates a typical crack in the fine microstructure tested at 140 MPa. In this case, three slip bands formed in close proximity and presumably experienced decohesion to varying degrees, as seen in Figure 11(a). Figure 11(b) shows that a crack evolved from the most-dominant slip band, departed from this slip

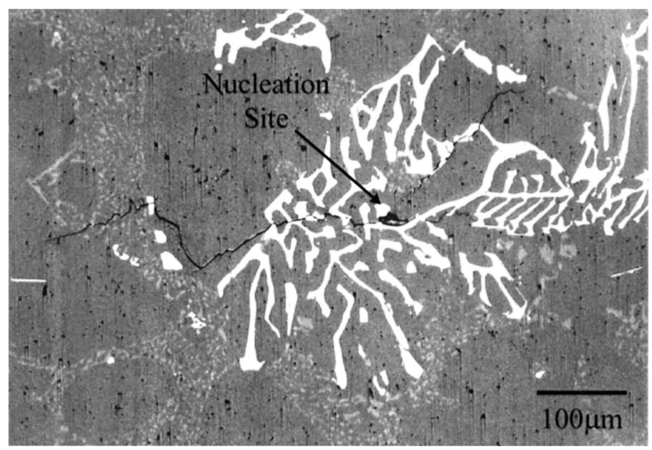

(*a*)

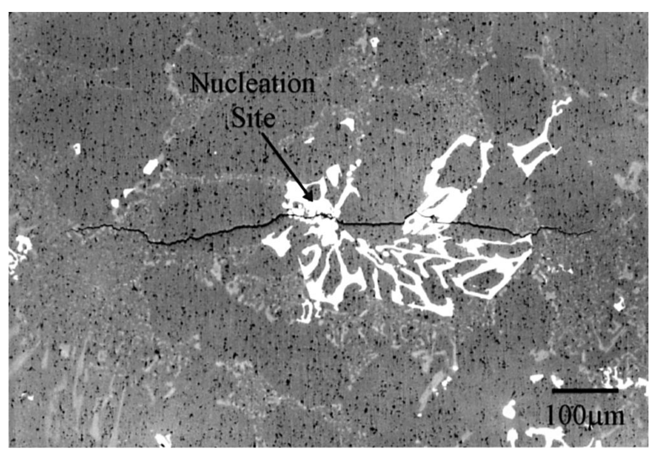

(*b*)

Fig. 9—SEM micrographs of fatigue cracks in the coarse microstructure. Both cracks initiated at the specimen surface and the arrows indicate the nucleation sites, both located at a large intermetallic script phase ($Al_{15}(Mn, Fe)_3Si_2$): (*a*) 56,017 cycles at 100 MPa and (*b*) 110,029 cycles at 100 MPa.

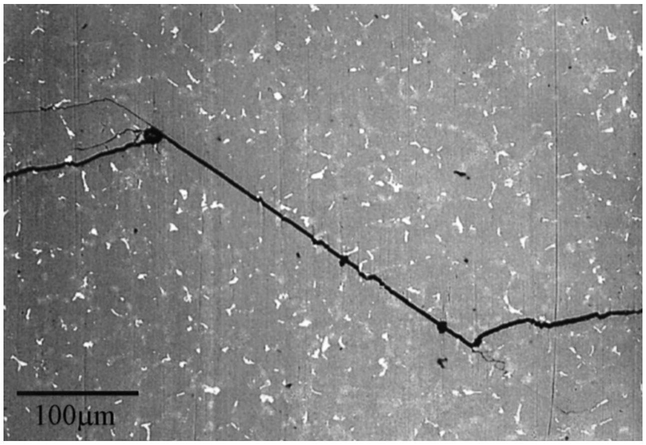

Fig. 10—SEM photograph showing a small fatigue crack that initiated from the formation and eventual decohesion of a slip band in the fine microstructure under a stress amplitude of 100 MPa. The crack departs from the slip band and propagates in a direction perpendicular to the loading direction.

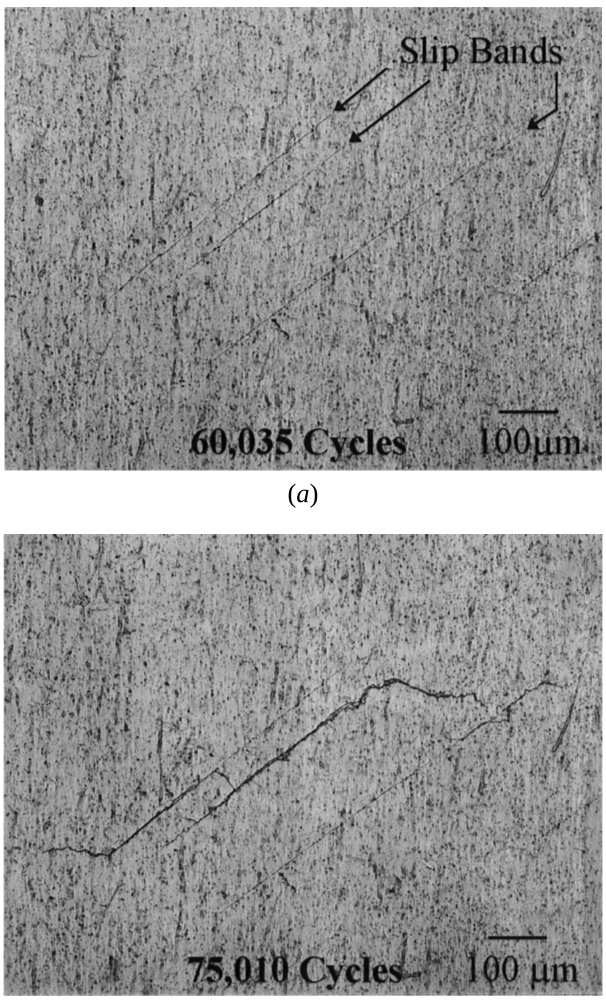

(*a*)

(*b*)

Fig. 11—(*a*) Acetate replica taken at 60,035 cycles showing slip bands that formed on the surface of a fine microstructure specimen at a stress amplitude of 140 MPa. (*b*) Acetate replica taken at 75,010 cycles showing the fatigue crack, which initiated from one of the slip bands, grew into two adjacent slip bands, and eventually propagated away from the slip bands in a direction perpendicular to the loading direction.

plane, grew approximately perpendicular to the loading direction, eventually linked the neighboring slip bands, and ultimately propagated away from the slip bands perpendicular to the loading direction. The presence of the slip bands indicates that plasticity around the propagating crack may be significant.

Multiple cracks formed on the specimen surfaces of both microstructures, in the tests conducted at the stress amplitude of 140 MPa. In these cases, growth measurements were taken from singular cracks growing independently, and cases of crack interaction and coalescence were not considered. At the 100 MPa stress amplitude, only one or two cracks were typically initiated in a specimen. This was true for both the fine and coarse microstructures.

D. *Crack Propagation*

Figure 12 compares the growth behavior of small and long cracks in both the coarse and the fine microstructural conditions of the cast W319 Al alloy. The solid curves represent the long-crack data obtained from the CT specimens. These curves combine the decreasing ΔK segment down to the threshold level and the increasing ΔK segment to failure. The individual data points represent the small cracks measured by replication and grown under constant-amplitude loading. It is apparent from Figure 12 that a small-crack effect occurs in both microstructures of this alloy. The long-crack data indicate threshold stress-intensity factors of 2.7 MPa$\sqrt{\text{m}}$ in the fine microstructure and 4.0 MPa$\sqrt{\text{m}}$ in the coarse microstructure. The solid and open triangles indicate the measured growth rates of small cracks in the fine microstructure at stress amplitudes of 140 and 100 MPa, respectively. These cracks propagated at ΔK levels as low as 0.7 MPa$\sqrt{\text{m}}$ at 140 MPa and 1.1 MPa$\sqrt{\text{m}}$ at 100 MPa, both significantly less than the measured long-crack ΔK_{th} level. The growth rates of the small cracks in the fine microstructure spanned an order of magnitude ranging from $\sim 7 \times 10^{-10}$ to 7×10^{-9} m/cycle. The solid and open circles indicate the measured growth rates of small cracks in the coarse microstructure at stress amplitudes of 140 and 100

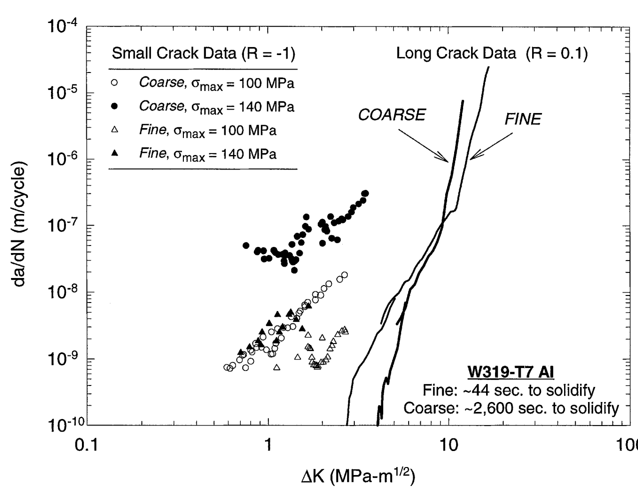

Fig. 12—Fatigue crack growth rate data for long and small cracks in the W319 aluminum alloy. A small crack effect is evident in this material. Small crack growth rates are dependent upon solidification rate and the applied stress amplitude when ΔK is used as a correlating parameter.

MPa, respectively. In this microstructure, small cracks propagated at ΔK levels as low as 0.8 MPa$\sqrt{\text{m}}$ at 140 MPa and 0.6 MPa$\sqrt{\text{m}}$ at 100 MPa, both significantly lower than the long-crack ΔK_{th} level. Small-crack growth rates in the coarse microstructure ranged from $\sim 7 \times 10^{-10}$ to 3×10^{-7} m/cycle. In both microstructures, small-crack growth measurements terminated (due to specimen fracture) at a ΔK level which was equal to or slightly lower than the respective long-crack ΔK_{th} level. At termination, small-crack growth rates were in the range of 2×10^{-9} to 2×10^{-7} m/cycle, as compared to the long-crack threshold growth rates of $<1 \times 10^{-10}$ m/cycle.

The small-crack data represent two to four different cracks monitored for each testing condition. Some of the cracks exhibit a region of decelerating growth rate with increasing levels of ΔK. This behavior is likely due to interaction of the crack front with local microstructural features that impede crack advancement, such as grain boundaries or interdendritic regions with enhanced stiffness. This effect is not commonly seen in long-crack data, since such local decelerations or accelerations are averaged over a much larger crack front and larger Δa value.

Comparing the small-crack data of the fine and coarse microstructures at a given stress amplitude indicates a distinct influence of solidification rate. At the stress amplitude of 100 MPa, small cracks propagated in the coarse microstructure at rates about half of one order of magnitude greater than in the fine microstructure. At the stress amplitude of 140 MPa, the difference in small-crack behavior in the two microstructures is more pronounced, with growth rates one order of magnitude faster in the coarse condition than in the fine condition, for a given δK level.

A stress-level effect can also be seen when comparing the small-crack data for a given microstructural condition. Figure 13 shows that small cracks in the fine microstructure propagate at higher rates (about half of one order of magnitude) under the higher stress amplitude of 140 MPa (69 pct σ_{yield}) than at the lower stress of 100 MPa (49 pct σ_{yield}). The influence of stress level is more pronounced in the coarse microstructure, as viewed in Figure 14, where approximately

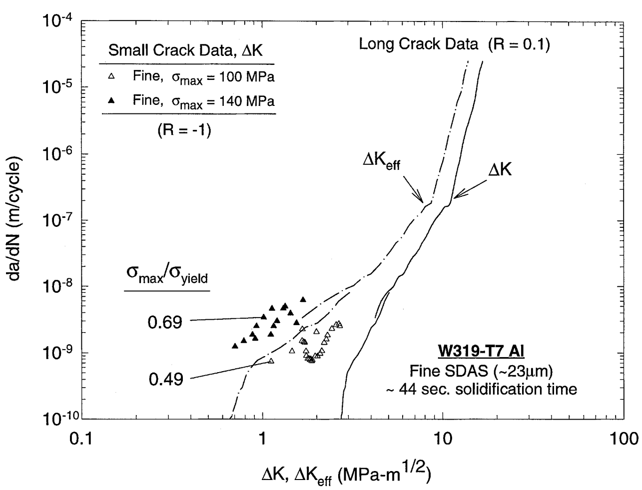

Fig. 13—Fatigue crack growth rate data for long and small cracks in the fine microstructure (solidification time ~44 s, 23 μm SDAS) of the W319 aluminum. The dash-dot curve represents the long-crack growth data corrected for crack closure where ΔK_{eff} was determined by the ASTM technique described in Ref. 18.

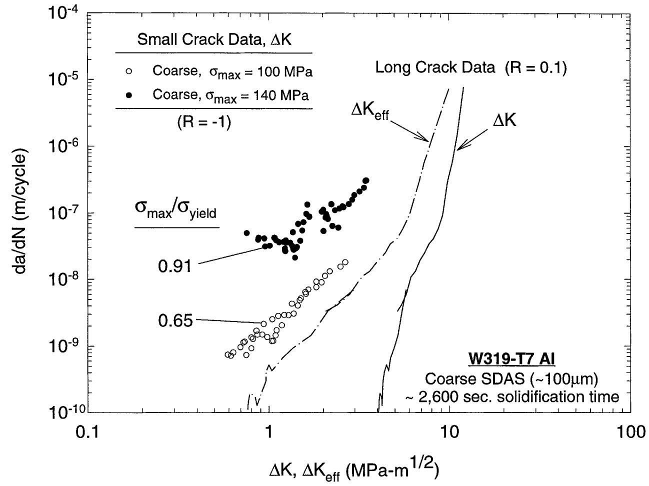

Fig. 14—Fatigue crack growth rate data for long and small cracks in the coarse microstructure (solidification time ~2600 s, 100 μm SDAS) of the W319 aluminum. The dash-dot curve represents the long-crack growth data corrected for crack closure where ΔK_{eff} was determined by the ASTM technique described in Ref. 18.

one order of magnitude greater growth rates were measured at the higher stress amplitude. In the coarse microstructure, the 100 and 140 MPa stress amplitudes constitute a greater fraction of the yield strength (65 and 91 pct σ_{yield}).

IV. DISCUSSION

A. *Crack Initiation*

This study represents an initial attempt to examine the growth of small fatigue cracks in a commercial cast aluminum alloy. It is well documented that, in cast aluminum, fatigue crack initiation occurs mainly at large microshrinkage pores or at clusters of smaller pores[1–4] which are distributed throughout the specimen volume. To facilitate the observation of crack initiation and early growth by replication and to allow us to focus on propagation, all castings were hot isostatically pressed to reduce porosity and its influence on crack initiation and to increase the likelihood of fatigue crack initiation at or very near specimen surfaces. Under these conditions, fatigue cracks initiated on or near the specimen surface and predominantly at large (~300 to 800 μm) script-phase intermetallics ($Al_{15}(Mn, Fe)_3Si_2$) in the coarse microstructure (Figure 9) and from slip bands that formed in the fine microstructure (Figures 10 and 11). Further studies will be required to evaluate the role of porosity and other microstructural features in crack initiation. For the present study, however, it is not anticipated that the propagation behavior is significantly influenced by changing the size and number of pores.

B. *Crack Propagation*

A substantial small-crack effect exists in the cast W319 alloy, as evident from the data in Figure 12. It can be noted that the small cracks were measured under fully-reversed loading ($R = -1$), while the long-crack data were obtained at a positive stress ratio of $R = 0.1$. However, the effect of the different stress ratios is thought to be small, since only the tensile portion of the loading cycle is believed to contribute to crack propagation. Also, if the long-crack data were acquired under a stress ratio of -1, then the extent of the small-crack effect would likely become more pronounced.

One of the proposed reasons for the anomalous fast growth of small cracks is reduced levels of crack closure. It is thought that a crack will only advance under opening or tensile-mode loading when its tip or front is open. In the case of large cracks, the crack front is not fully open over the entire range of the loading cycle. A certain tensile stress must be reached before the crack begins to be fully open (σ_{op}), due to the wake of plastically deformed material surrounding the crack, roughness of the mating crack surfaces, the formation of oxides on the exposed crack surfaces, or a combination of these three factors. The effective stress range over which the crack can advance is then reduced to

$$\Delta\sigma_{\text{eff}} = \sigma_{\max} - \sigma_{op} \qquad [4]$$

Incorporating the effective stress range of Eq. [4] into the stress-intensity-factor range yields a reduced crack-driving parameter. A small crack, on the other hand, should not experience the same degree of closure, since it has not yet developed a significant envelope of plastically deformed material or a sufficient area fraction of asperities. Figures 13 and 14 show long-crack growth rates as a function of ΔK and ΔK_{eff} in the fine and coarse microstructures, respectively. Included in these two figures are the small-crack data for the respective microstructures at the two stress amplitudes of 100 and 140 MPa. Consideration of crack closure is seen to shift the long-crack data closer to the small-crack growth rates, where the difference between long-crack ΔK and ΔK_{eff} curves becomes progressively more pronounced at the near-threshold regime. In the case of the fine microstructure (Figure 13), the long-crack closure-corrected curve estimates growth rates somewhere between the small-crack rates measured at the stress amplitudes of 49 and 69 pct σ_{yield}. The long-crack ΔK_{eff} curve estimates small-crack growth rates $\sim$1 to 3 times slower than the small cracks measured at the higher stress amplitude and $\sim$1 to 3 times faster than those measured at the lower stress amplitude. In the case of the coarse microstructure (Figure 14), the ΔK_{eff} curve approaches the small-crack data but registers growth rates slightly less than the small cracks at the 100 MPa (65 pct σ_{yield}) stress amplitude and between one and two orders of magnitude less than the small cracks at the 140 MPa (91 pct σ_{yield}) stress amplitude. Figures 13 and 14 suggest that while crack closure contributes to the difference between the growth rates of small and long cracks, it cannot solely account for the small-crack effect in this alloy.

Stress amplitude displays a strong influence on the small-crack growth curves but has no effect on the long-crack data. The influence of stress level on the growth rate of small cracks can be attributed to the scale of yielding at the crack tip. Implicit when using the LEFM parameter ΔK to correlate crack growth is the assumption of small-scale yielding, where the plastic zone size attendant at the crack tip is small in relation to the dimensions of the crack. For small cracks, this assumption can be violated to varying degrees depending upon the applied stress level and the yield strength of the material. It has been suggested that the growth rate of a small fatigue crack is proportional to the extent of plastic deformation at the crack tip.[22] This phenomenon is presumed to result in the higher growth rates at higher ratios of $\sigma_{\max}/\sigma_{\text{yield}}$ observed in W319 aluminum, as shown in Figures 13 and 14, and, along with reduced closure levels, serves as a contributing factor to the small-crack effect. A stress-level effect on the growth of small cracks has been observed by other investigators. Newman and Edwards report a distinct dependence of small-crack growth on the applied-stress amplitude in a 2024-T3 aluminum alloy.[23] They further observed that the magnitude of the stress-level effect depended upon the stress ratio. The effect was most pronounced for negative R values, was smaller for $R = 0$, and stress had no effect at positive R values. It can be inferred from this observation that the compressive portion of the loading cycle significantly increases the degree of plasticity at the crack tip. It could also be postulated that the compressive cycle may effectively deform the irregular features on the mating crack surfaces, imparting a kind of smoothing effect similar to that seen as a result of periodic compressive overloads.[24] This would reduce the shielding contribution from roughness-induced crack closure. The degree to which these phenomena contribute to the stress-level effect is not known. A stress-level effect on the rate of small-crack growth has also been observed by O'Connor and Plumtree[13] in a squeeze-cast 6066-T6 aluminum alloy tested under fully reversed loading ($R = -1$). Gungor and Edwards,[14] on the other hand, observed no discernible stress-level effect on the growth rate of small cracks in a squeeze-cast 6082-T6 aluminum alloy. However, their experiments were conducted under a positive stress ratio ($R = 0.1$).

In their study of 6082-T6 aluminum, Gungor and Edwards[14] showed that the elastic ΔK solution given in Eq. [3] provided a unique definition of small-crack growth rates tested at different stress levels. That is, small-crack growth data measured at six different stress amplitudes ranging from 105 to 150 MPa (40 to 57 pct σ_{yield}) fell with relative consistency on a single line when plotting da/dN *vs* ΔK. They then predicted fatigue life through integration of the Paris equation using the single set of constants determined from the small-crack data and obtained excellent agreement with experimental results at lives less than 2×10^5 cycles. However, the success of this approach to life prediction is enabled by the absence of any significant stress-level dependence in the da/dN *vs* ΔK data. For applications with zero or negative stress ratios, ΔK does not necessarily provide a unique correlation to small-crack growth rates. As the small-crack data in Figures 13 and 14 illustrate, a single Paris relation is not adequate to define growth at different applied-stress amplitudes. The significant dependence on stress amplitude requires that a series of data be established over a range of stress levels, or that some predictive method be devised by which small-crack growth rates over a range of stress levels can be accurately estimated. In order to practically incorporate small-crack growth behavior into a material model or a life prediction model, a driving parameter is sought which can uniquely define the growth rates at different stresses. Optimally, a driving parameter which can also predict microstructural (solidification-rate) effects is desired. This could require a modified version of ΔK or a correlating parameter other than ΔK.

Since the assumption of small-scale yielding is violated for small fatigue cracks, an elastic-plastic stress-intensity-factor range (ΔK_p) may serve as a more appropriate driving parameter than the elastic ΔK solution for correlating small-crack propagation.[25] The definition of ΔK_p differs from that of ΔK by incorporating the degree of plastic deformation attendant at the crack tip and can be expressed in a form similar to that of Eq. [3] as

$$\Delta K_p = \Delta\sigma \cdot F \cdot \sqrt{\frac{\pi}{Q}(a + \gamma\rho)} \qquad [5]$$

Here, the size of the crack is effectively augmented by some factor of the cyclic plastic-zone size (ρ). The term γ can be assumed constant and has been assigned values ranging from 0.25 to 1, depending upon crack configuration, as reported in Reference 25. The value of ρ is calculated using a modified Dugdale approach, expressed as

$$\rho = a\left(\sec\left(\frac{\pi\sigma_{\max}}{2\sigma_o}\right) - 1\right) \qquad [6]$$

where σ_o represents the flow stress and is calculated as the average of the yield and ultimate tensile strengths. The elastic-plastic parameter ΔK_p should serve to correct for stress-level effects, in that load conditions with greater values of $\sigma_{\max}/\sigma_o$ will be assigned a driving parameter of greater magnitude. That is, plotting *da/dN vs* ΔK_p will shift the small-crack data in Figures 13 and 14 to the long-crack curves, with the shift being greater for the data acquired at higher stress amplitudes. Figure 15 shows the small-crack data as a function of the elastic-plastic parameter ΔK_p, as well as the closure-corrected long-crack data plotted as a function of ΔK_{eff}. This figure shows that ΔK_p is effective in reducing the stress-level effect in the small-crack data for the coarse microstructure and brings these data into closer agreement with the long-crack ΔK_{eff} curve. The influence of ΔK_p on the data for the fine microstructure is minimal. Despite the improved correlation of the data for the coarse condition, there remains a distinct stress-level effect for both microstructural conditions when using this elastic-plastic analysis.

Nisitani *et al.*[26] have suggested that the following relation can be used to successfully correlate the growth of small fatigue cracks under high nominal stresses where large-scale yielding is attendant:

$$\frac{da}{dN} = C_1\sigma_a^n a \qquad [7]$$

Here, C_1 and n are constants and σ_a is the stress amplitude. This type of crack-growth relation was proposed previously by Frost and Dugdale[27] and was shown to correlate the growth behavior of long cracks in a mild steel and aluminum alloy (BS.L71). Nisitani *et al.* explain that an appropriate parameter for determining the propagation rate of a crack is the crack-tip opening displacement (CTOD), which is closely related to the cyclic plastic zone size. Equation [7] is based upon the assumption that the propagation rate of a crack is proportional to the size of its plastic zone, which, in turn, depends upon the stress level and crack length. Figure 16 shows the measured small-crack growth rates as a function of $\sigma_a^n a$, where an exponential term (n) of 7 was determined by trial and error to give the best fit of the data. This approach appears to uniquely define the growth rates within the individual microstructures at both stress amplitudes. That is to say, the growth data for the coarse microstructure tested at 100 and 140 MPa fall, within reasonable scatter, on a single curve, as do the data for the fine microstructure at these two stress amplitudes. This is a compelling result, as it suggests that a single curve may define the growth behavior of small cracks in a given microstructure over a wide range of stress amplitudes. This is a feature that ΔK and ΔK_p are unable to supply, at least at this negative stress ratio. It is also encouraging that the growth curves in Figure 16 appear to be linear. The propagation life of a small fatigue crack can be estimated by integrating the curve from some initial crack size (a_i) to the critical size to cause failure (a_f). If the crack has initiated in a laboratory specimen, then it is likely that a_f will be relatively small, and Eq. [7] will apply over the entire propagation life.

In using the function $\sigma_a^n a$, Figure 16 shows that there remains a distinct difference in growth behavior between the coarse and fine microstructures. At a given value of $\sigma_a^n a$, faster growth occurs in the coarse microstructure. This

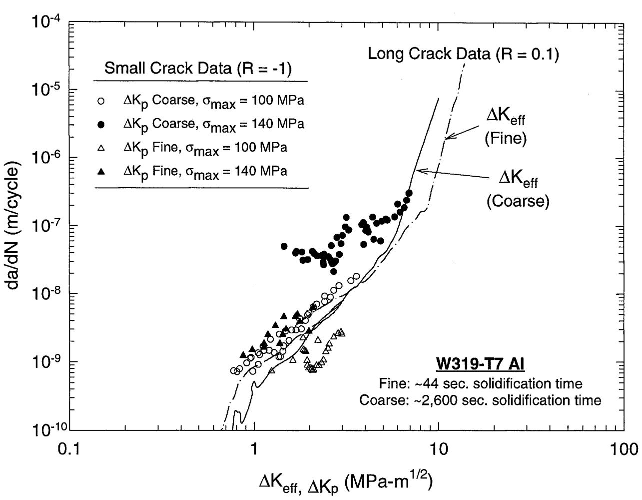

Fig. 15—Small-crack growth data in the coarse and fine microstructures as a function of an elastic-plastic stress intensity parameter (ΔK_p) plotted with the long-crack data as a function of the closure-corrected elastic stress intensity parameter (ΔK_{eff}).

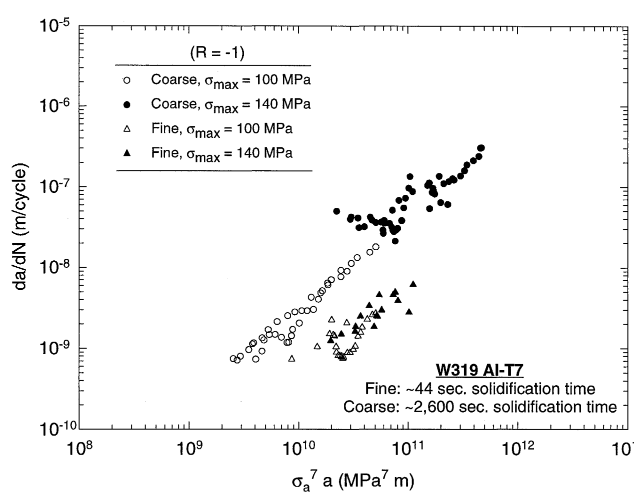

Fig. 16—Small-crack growth rates for both the fine and coarse microstructures at stress amplitudes of 100 and 140 MPa correlated with the parameter given in Eq. [7]. An exponential value of 7 gave the best empirical fit of the data.

is a reasonable result since, as Figure 8 clearly illustrates, the strengths of these two microstructures differ considerably. To compare the growth data of different materials, Nisitani *et al.*[26] suggest modifying Eq. [7] to include material properties such as σ_{yield} or the ultimate tensile strength. Equation [7] can be modified to the form

$$\frac{da}{dN} = C_2\left(\frac{\sigma_a}{\sigma_B}\right)^n a \qquad [8]$$

where σ_B can represent σ_{yield} or σ_t. An attractive feature of Eq. [8] is that the term within parentheses, which is raised to some exponential power, is dimensionless. The driving parameter in this case is, therefore, in units of length. Shiozawa *et al.*[12] have shown that small fatigue crack growth in two squeeze-cast aluminum alloys (AC8A-T6 and AC4C-T6) is correlated well by the parameter $((\sigma_a/\sigma_t)^n a)$, where an n value of 4.8 gave the best fit of the data. It was found that using ultimate tensile strength as the normalizing term σ_B in Eq. [8] is not effective in eliminating the influence of the microstructural condition on the growth data for the W319 alloy. However, incorporating the yield strength of the coarse and fine conditions of the W319 alloy into the correlating parameter of Eq. [8] provides better results. Figure 17 shows the small-crack growth data of the W319 alloy as a function of the term $(\sigma_a/\sigma_{\text{yield}})^n a$, where a value of $n = 7$ gave the best fit of the data. It is seen that this function successfully correlates the growth rates at different stress levels in the individual microstructures, and the influence of the microstructural condition is essentially eliminated within the scatter of the growth data. While this parameter shows a considerable improvement in the correlation of the small-crack data over an elastic ΔK solution, there is still scatter in the data, which shows up to a factor-of-5 difference in growth rates for a given driving force. However, within this scatter, there is no evidence of a strong influence of applied stress level nor solidification rate. This is an encouraging result, as it suggests that a correlating parameter like that given in Eq. [8] could be effective in characterizing small-crack growth for a wide range of applied stresses and also for a wide range of solidification conditions.

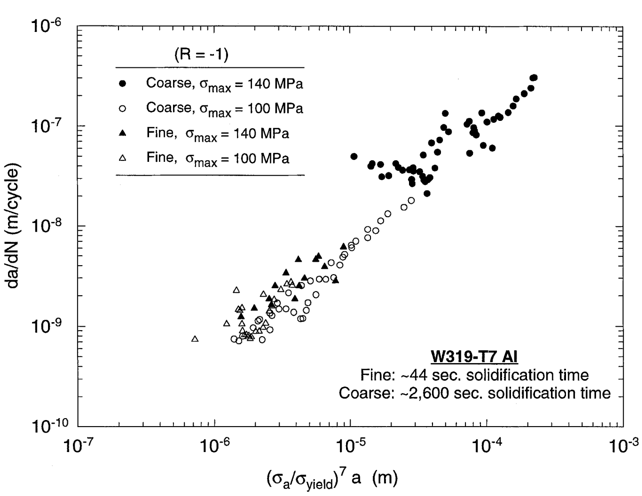

Fig. 17—Small crack growth rates for both the fine and coarse microstructures at stress amplitudes of 100 and 140 MPa correlated with a parameter that incorporates the yield strength of the respective microstructures (Eq. [8]). An exponential value of 7 gave the best empirical fit of the data.

The simplicity of Eq. [8] is attractive from a practical standpoint. However, the physical significance of this correlating parameter is not fully understood. In comparing the driving force for crack propagation in two different materials based upon the concept of CTOD, the parameter in Eq. [8] may be omitting an important consideration. It is thought that the effect of solidification rate on the growth behavior of the small cracks is closely related to the difference in strength between the two microstructures. Simply stated, a stronger microstructure will present more resistance to crack-tip opening by allowing less plastic deformation at the crack tip. As explained in Reference 26, the correlating parameter in Eq. [7], $\sigma_a^n a$, accounts for crack-tip plasticity by relating the cyclic plastic-zone size to the applied-stress amplitude and the crack size. The correlating parameter in Eq. [8], $(\sigma_a/\sigma_{\text{yield}})^n a$, attempts to normalize the degree of crack-tip plasticity by including the yield-strength term and allows comparison of materials with different strengths. Another contribution to CTOD not yet considered is the global deformation imparted on a specimen during the loading cycle. A greater tensile deformation of the continuum surrounding a crack tip will result in a greater CTOD. Looking closely at the stress-strain curves of the two microstructures in Figure 8, it can be seen that both curves depart from linear elastic behavior significantly below their calculated 0.2 pct offset yield strengths, and significantly different strains are imparted at equivalent stress levels. In light of this, it may be important to consider the total strain of a specimen when evaluating the effect of CTOD on propagation. Taking this into consideration, Eq. [8] can be rewritten as

$$\frac{da}{dN} = C_3\left(\varepsilon_{\max} \cdot \frac{\sigma_a}{\sigma_{\text{yield}}}\right)^n a \qquad [9]$$

where $\varepsilon_{\max}$ is the maximum total strain achieved during the loading cycle. As in Eq. [8], the term within parentheses is dimensionless and the function correlating crack growth, $(\varepsilon_{\max}\ \sigma_a/\sigma_{\text{yield}})^n a$, is in units of length. The values of $\varepsilon_{\max}$ at the two stress amplitudes (100 and 140 MPa) were determined from the data represented in Figure 8 and are reported for both microstructures in Table III. It should be noted that these values were obtained for monotonic, not cyclic, loading. Cyclic stress-strain curves have not been established at this time.

Figure 18 shows the small-crack growth rates as a function of $(\varepsilon_{\max}\ \sigma_a/\sigma_{\text{yield}})^n a$, where an exponential value of $n = 2.5$ was determined to give the best fit of the data. This correlating parameter, like that in Eq. [8], provides good correlation of the small-crack data. Within the scatter of the data, there is little discernible influence of solidification condition or stress level. However, correlation with the parameter $(\sigma_a/\sigma_{\text{yield}})^n a$ in Figure 17 appears to give a slightly better collapse

Table III. The Maximum Strains, $\varepsilon_{\max}$, Achieved in the Fine and Coarse Microstructures at the 100 and 140 MPa Stress Amplitudes

	Maximum Total Strain, $\varepsilon_{\max}$ (m/m)	
Stress Amplitude	Fine	Coarse
100 (MPa)	1.25×10^{-3}	1.65×10^{-3}
140 (MPa)	1.93×10^{-3}	3.39×10^{-3}

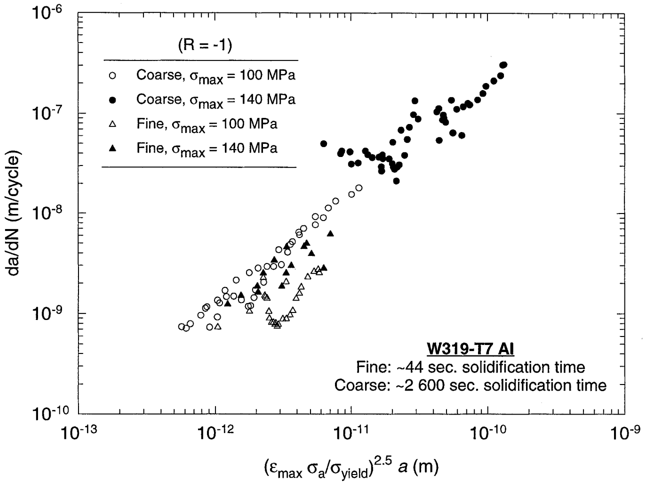

Fig. 18—Small crack growth rates for both the fine and coarse microstructures at stress amplitudes of 100 and 140 MPa correlated with a parameter that includes terms for yield strength, σ_{yield}, and ductility, ε_{max} (Eq. [9]). An exponential value of 2.5 gave the best empirical fit of the data.

of the small-crack data. Still, the strain imparted upon the specimen may be an important consideration when comparing crack advance in different materials with different responses to applied loads.

The good correlation of small-crack growth data achieved in Figures 17 and 18 is an encouraging step toward obtaining an accurate material model, which will be sensitive to such variables as solidification rate and applied-stress amplitude when predicting fatigue properties of cast W319 specimens. It appears that a single expression could characterize small-crack propagation behavior for a wide range of solidification conditions and a wide range of applied-stress amplitudes. However, with the limited amount of small-crack data currently available, it is difficult to know the range of material and testing conditions over which Eqs. [8] and [9] are applicable. Further study is required to address whether the parameters $(\sigma_a/\sigma_{yield})^n a$ and $(\varepsilon_{max}\ \sigma_a/\sigma_{yield})^n a$ will provide good correlation for other solidification rates and stress amplitudes, as well as variations in heat treatment, grain refinement, and stress ratio.

V. CONCLUSIONS

The following conclusions can be made from this investigation of small fatigue crack behavior in a cast W319 Al alloy.

1. Fatigue cracks as small as 17 μm were reliably measured by a replication technique in specimens machined from a cast W319 aluminum alloy. The specimens were taken from hot isostatically pressed material in order to reduce porosity and promote crack initiation at or very near the specimen surface.
2. A significant small-crack effect was observed in this alloy. That is, all of the small cracks measured grew substantially faster than the long cracks when compared using a linear elastic stress-intensity-factor range as the correlating parameter for crack growth.
3. A stress-level effect was evident in the small-crack growth curves for both the fine and coarse microstructures, when using an LEFM analysis. Small cracks grew faster through both microstructures at the higher applied-stress amplitude (σ_{max} = 140 MPa) than at the lower applied-stress amplitude (σ_{max} = 100 MPa). This effect was most pronounced in the lower-strength, coarse microstructural condition.
4. The rate at which the cast material solidifies significantly influences the propagation behavior of small fatigue cracks. It was observed that, under equivalent applied-stress amplitudes, small cracks grew much faster through the lower-strength, coarse microstructure than through the higher-strength, fine microstructure for the same calculated ΔK level. The difference in small-crack growth rates between the two microstructural conditions was more pronounced for tests conducted under the higher applied-stress amplitude (σ_{max} = 140 MPa) and was as great as one order of magnitude in some cases.
5. Correlating parameters of the form $(\sigma_a/\sigma_{yield})^n a$ and $(\varepsilon_{max}\ \sigma_a/\sigma_{yield})^n a$ were shown to characterize the small-crack growth data with little discernible influence of solidification condition or stress amplitude.

REFERENCES

1. M.J. Couper, A.E. Neeson, and J.R. Griffiths: *Fatigue Fract. Eng. Mater. Struct.*, 1990, vol. 13(3), pp. 213-27.
2. B. Skallerud, T. Iveland, and G. Harkegard: *Eng. Fract. Mech.*, 1993, vol. 44 (6), pp. 857-74.
3. J.M. Boileau and J.E. Allison: *Fatigue '96 Proc. 6th Int. Fatigue Congr.*, 1996, Elsevier Science, Inc., Tarrytown, NY, vol. 2, pp. 941-46.
4. C.-H. Ting: Ph.D. Dissertation, University of Illinois at Urbana–Champaign, Urbana, 1991.
5. R.O. Ritchie and J. Lankford: *Small Fatigue Cracks*, TMS, Warrendale, PA, 1986.
6. J. Larsen and J.E. Allison: *Small-Crack Test Methods*, ASTM, Philadelphia, PA, 1992.
7. J.C. Newman, Jr., E.P. Phillips, and M.H. Swain: NASA Technical Memorandum No. 110307, NASA, Washington, DC, 1997.
8. K. Tanaka and Y. Akiniwa: *Fatigue '96 Proc. 6th Int. Fatigue Congr.* 1996, Elsevier Science, Inc., Tarrytown, NY, pp. 27-38.
9. P.R. Edwards and J.C. Newman, Jr.: AGARD Report No. 767, AGARD, 1990.
10. S. Pearson: *Eng. Fract. Mech.*, 1975, vol. 7(2), pp. 235-47.
11. W.L. Morris, M.R. James, and O. Buck: *Metall. Trans. A*, 1981, vol. 12A, pp. 57-64.
12. K. Shiozawa, Y. Tohda, and S.-M. Sun: *Fat. Fract. Eng. Mater. Struct.*, 1997, vol. 20 (2), pp. 237-47.
13. B.P.D. O'Connor and A. Plumtree: *Fatigue '87*, 1987, EMAS (Engineering Materials Advisory Services, Ltd., West Midlands, U.K., vol. 1, pp. 145-54.
14. S. Gungor and L. Edwards: *Fat. Fract. Eng. Mater. Struct.*, 1993, vol. 16(4), pp. 391-403.
15. M.E. Seniw, M.E. Fine, E.Y. Chen, M. Meshii, and J. Gray: *Proc. High Cycle Fatigue of Structural Materials: Paul Paris Symp. Materials Week '97*, Indianapolis, IN, Sept. 14–18, 1997, TMS, Warrendale, PA, 1998.
16. W. Elber: *Damage Tolerance in Aircraft Structures*, ASTM, Philadelphia, PA, 1971, pp. 230-42.
17. M.H. El Haddad, K.H. Smith, and T.M. Topper: *J. Eng. Mater. Technol.*, 1979, vol. 101, pp. 42-46.
18. K. Donald: *Mechanics Fatigue Crack Closure*, ASTM, Philadelphia, PA, 1988, pp. 222-29.
19. R.E. Peterson: *Stress Concentration Factors*, Wiley Co., New York, NY, 1974, p. 37.
20. M.H. Swain: *Small-Crack Test Methods*, ASTM, Philadelphia, PA, 1992, pp. 34-56.
21. J.C. Newman, Jr. and I.S. Raju: *Eng. Fract. Mech.*, 1981, vol. 15, pp. 18-92.
22. L. Edwards and Y.H. Zhang: *Acta Metall. Mater.*, 1994, vol. 42 (4), pp. 1413-21.
23. J.C. Newman, Jr. and P.R. Edwards: AGARD Report No. 732, AGARD, 1988.

24. A. Varvani-Farahani and T.H. Topper: *Fatigue '96 Proc. 6th Int. Fatigue Congr.*, 1996, pp. 295-300.
25. J.C. Newman, Jr.: *Small-Crack Test Methods*, ASTM, Philadelphia, PA, 1992, pp. 6-33.
26. H. Nisitani, M. Goto, and N. Kawagoishi: *Eng. Fract. Mech.*, 1992, vol. 41 (4) pp. 499-513.
27. N.E. Frost and D.S. Dugdale: *J. Mech. Phys. Solids*, 1958, vol.6, pp. 92-110.